

Fourier phase-demodulation applied to strip-light 360-degrees profilometry of 3D solids; theoretical principles

Manuel Servin, Moises Padilla and Guillermo Garnica

*Centro de Investigaciones en Optica A. C., 115 Loma del Bosque,
Col. Lomas del Campestre, 37150 Leon Guanajuato, Mexico.*

October 2015

mservin@cio.mx

Abstract: 360-degrees digitalization of three-dimensional (3D) solids using a projected light-strip is a well established technique. These profilometers project a light-strip over the solid under analysis while the solid is rotated a full revolution. Then a computer program typically extracts the centroid of this light-strip, and by triangulation one obtains the shape of the solid. Here instead of using intensity-based strip centroid estimation, we propose to use Fourier phase-demodulation. This 360-degrees profilometer first constructs a carrier-frequency fringe-pattern by closely adding individual light-strip images. Secondly this high-density fringe-pattern is phase-demodulated using the standard Fourier technique.

OCIS codes: (120.0120) Instrumentation, measurement, and metrology; (120.5050) Phase measurement; (120.4630) Optical inspection

References and links

1. M. Takeda, H. Ina, S. Kobayashi, "Fourier-transform method of fringe-pattern analysis for computer-based topography and interferometry," *J Opt. Soc. Am. A* **72**, 156–60 (1982).
 2. M. Halioua, R. S. Krishnamurthy, H. C. Liu, and F.P. Chiang, "Automated 360° profilometry of 3-D diffuse objects," *Appl. Opt.* **24**, 2193-2196 (1985).
 3. X. X. Cheng, X. Y. Su, and L. R. Guo, "Automated measurement method for 360° profilometry of 3-D diffuse objects," *Appl. Opt.*, **30**, 1274-1278 (1991).
 4. A. K. Asundi, "360-deg profilometry: new techniques for display and acquisition," *Opt. Eng.* **33**, 2760-2769 (1994).
 5. M. Chang, W. C. Tai, "360-deg profile noncontact measurement using a neural network," *Opt. Eng.* **34**, 3572-3576 (1995).
 6. A. S. Gomes, L. A. Serra, A. S. Lage, A. Gomes, "Automated 360 degree profilometry of human trunk for spinal deformity analysis," in *Proceedings of Three Dimensional Analysis of Spinal Deformities*, M. Damico et al. eds., (IOS, Burke, Virginia USA, 1995), pp. 423-429.
 7. Y. Song, H. Zhao, W. Chen, and Y. Tan, "360 degree 3D profilometry," *Proc. SPIE* **3204**, 204-208 (1997).
 8. A. Asundi and W. Zhou, "Mapping algorithm for 360-deg profilometry with time delayed integration imaging," *Opt. Eng.* **38**, 339-344 (1999).
 9. X. Su and W. Chen, "Fourier transform profilometry: a review," *Opt. and Lasers in Eng.* **35**, 263–284 (2001).
 10. X. Zhang, P. Sun, H. Wang, "A new 360 rotation profilometry and its application in engine design," *Proc. SPIE* **4537**, 265-268 (2002).
 11. J. A. Munoz-Rodriguez, A. Asundi, R. Rodriguez-Vera, "Recognition of a light line pattern by Hu moments for 3-D reconstruction of a rotated object," *Opt. & Laser technology* **37**, 131-138 (2005).
 12. G. Tmjillo-Schiaffino, N. Portillo-Amavisca, D. P. Salas-Peimbert, L. Molina-de la Rosa, S. Almazan-Cuellarand, L. F. Corral-Martinez, "Three-dimensional profilometry of solid objects in rotation," in *AIP Proceedings* **992**, 924-928 (2008).
 13. B. Shi, B. Zhang, F. Liu, J. Luo, and J. Bai, "360° Fourier transform profilometry in surface reconstruction for fluorescence molecular tomography," *IEEE Journal Biomed. Health Inf.* **17**, 681-689 (2013).
 14. Y. Zhang and G. Bu, "Automatic 360-deg profilometry of a 3D object using a shearing interferometer and virtual grating," *Proc. SPIE* **2899**, 162-169 (1996).
 15. M. Servin, G. Garnica, J. C. Estrada, and J. M. Padilla, "High-resolution low-noise 360-degree digital solid reconstruction using phase-stepping profilometry," *Opt. Exp.* **22**, 10914-10922 (2014).
-

1. Introduction

Fringe projection profilometry of three dimensional (3D) solids using Fourier phase-demodulation is well known since the classical paper by Takeda et al. in 1982 [1]. Although this phase-measuring technique effectively demonstrated that 3D digitalization was possible using a single carrier-frequency fringe-pattern, it cannot digitize the 360 degrees (360°) view of the 3D solid. As far as we know this was first implemented by Halioua et al. in 1985 [2]. He used a linear fringe-pattern projection with a 3-step phase shifter and a turntable to obtain the 360 degrees profilometry of a mannequin head [2]. Later in 1991, Cheng et al. achieved depth estimation by the use of an artificial-neural network projecting a laser strip over a solid lying in a turntable [3]. Single laser-strip profilometers use triangulation-based height estimation [3], which (in general) are less accurate than phase demodulation of high-density, carrier-frequency fringe-patterns [1-2]. Asundi published a fast 360 degrees technique based on a stroboscope strip-light projection and a digital drum camera rotating the solid at 2500 rpm [4]. Chang et al. used laser light-strip [5] and reconstructed a solid with 360-degrees using a neural network to estimate the center of the strips. Gomes et al. projected a linear-grating to analyze the spinal deformities of a human; they used Fourier profilometry [6]. Later on Song et al. used a fringe grating projector and phase-shifting interferometry to obtain the 360-degree object [7]. Asundi et al. also implemented a very fast 360 degrees profilometer using a time delay integration imaging for digitalization [8]. The state of the art on 3D profilometry was reviewed in 2001 by Sue and Chen but they have just included a single paper of 360-degrees profilometry [9]. More recently Zhang et al. have used 360 degrees profilometry for flow analysis in mechanical engines [10]. In 2005 Munoz-Rodriguez et al. used triangulation for 3D object reconstruction by projecting a strip-light and Hu moments [11]. In 2008 Trujillo-Shiaffino et al. used 360-degrees profilometry based on strip-light projection and triangulation to digitize a smooth rotation-symmetric object [12]. More recently Shi et al. used 360-degrees profilometry applied to fluorescent molecular tomography [13]. Some researchers have used shearing interferometry to project high quality linear fringes for 360-degrees profilometry [14]. This is a self-contained view of the main ideas behind 360° profilometry to this date.

Here we describe the theoretical aspects of a 360-degree profilometer using a projected light-strip over the 3D-solid under analysis. We take N CCD-images of the projected line over the 3D-solid for each rotating angle-step. In other words, for each rotation angle-step one takes one camera-image while the solid is rotated a full 360-degrees revolution. With these N -images set, a carrier-fringe pattern is constructed. This resulting carrier-frequency fringe-pattern is finally analyzed using the Fourier phase-demodulation technique.

2. 360° profilometers which uses a light-strip projection

Due to the light-strip projection geometry shown in Fig. 1 one minimizes the self-occluding shadows cast over the sphere shown. This is a great advantage of light-strip 360° -degree profilometry. In contrast, the fringe-projection 360° profilometry in Ref. [2] cast more self-occluding shadows over the digitizing solids. Probably this is the reason why the technique in [2] has lower popularity than light-strip 360° profilometry. In any 360° profilometer, the solid (the sphere in Fig. 1) must be positioned over a turntable and rotated 360° in the azimuthal angle φ to obtain the 3D-surface data from all possible 360° perspectives.

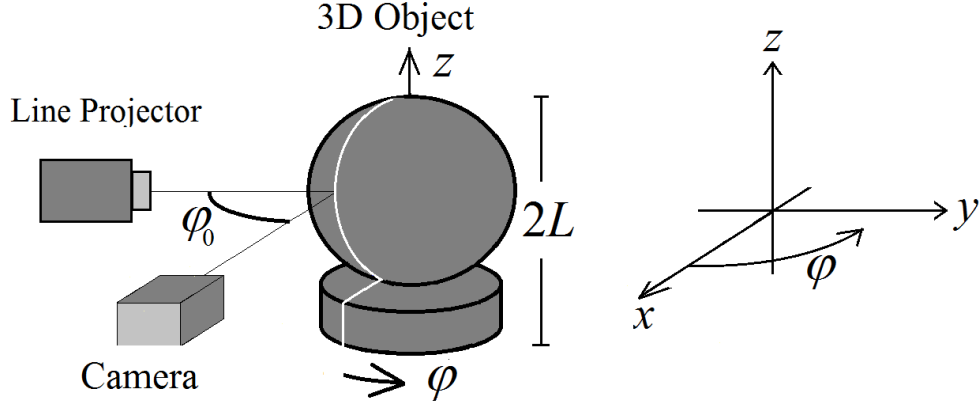


Fig. 1. This figure shows the light-strip profilometer with height-sensitivity $g=\sin(\phi_0)$; with this set-up, the self-occluding shadows are minimized. From N -camera images a single carrier fringe-pattern is obtained which can be phase-demodulated using the Fourier technique. Please note that the viewing point of this figure it is not the camera's perspective.

A mathematical model for the intensity of a light-strip as imaged over the digitizing CCD camera plane $(y, z) \in \mathbb{R}^2$ may be the following Gaussian irradiance (Figs. 1-3),

$$G(y, z; \phi) = \left\{ a(y, z; \phi) + b(y, z; \phi) e^{\frac{-[y-y(\phi, z)]^2}{\sigma^2}} \right\} \Pi(y); \quad g = \sin(\phi_0), \phi \in [0, 2\pi). \quad (1)$$

Where $y(\phi, z)$ is the strip-light phase displacement shown in Fig. 2 and Fig. 3. The profilometry sensitivity is given by $g = \sin(\phi_0)$. The window function $\Pi(y)$ is an indicator relation (Fig. 2 and Fig. 3) which may be expressed as,

$$\Pi(y) = \begin{cases} 1 & \text{if } y \in [0, -\max[y(\phi, z)]] \\ 0 & \text{otherwise} \end{cases}; \quad \phi \in [0, 2\pi], \quad z \in [-L, L]. \quad (2)$$

The camera takes the image of $G(y, z; \phi)$ as Fig. 2 shows. The center of the light-strip irradiance $y(\phi, z)$ is phase-modulated by the solid $y(\phi, z) = \sin(\phi_0)\rho(\phi, z)$ for each rotation-step $\Delta\phi$. The experimental image in Fig. 2 is formed at the CCD-camera plane corresponding to the schematics in Fig. 1 and Fig. 3.

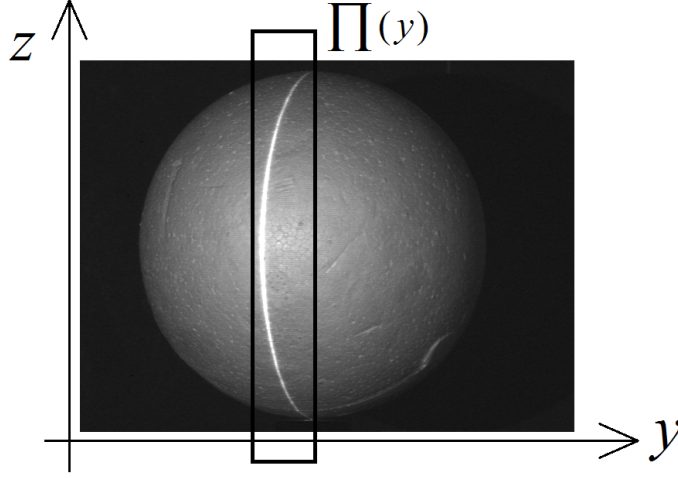


Fig. 2. A solid-sphere as imaged over the CCD-camera using a light-strip 360° profilometer. Each 360° full-digitalization, assuming a 1-degree rotation-step, needs 360 of these images. The light-strip projector is positioned as Fig. 1 shows; 360 strips (inside the square) are needed. In this figure, the ambient light is turned-on to show the digitizing sphere.

Figure 3 shows the sensitive angle φ_0 and the radius $\rho(\varphi, z_0)$ where the strip-light illuminates the solid. The distance $y(\varphi) = y(\varphi, z_0)$ is the phase-displaced strip-light as viewed from the camera. As mentioned, the mathematical relation among these functions is $y(\varphi, z) = \rho(\varphi, z) \sin(\varphi_0)$.

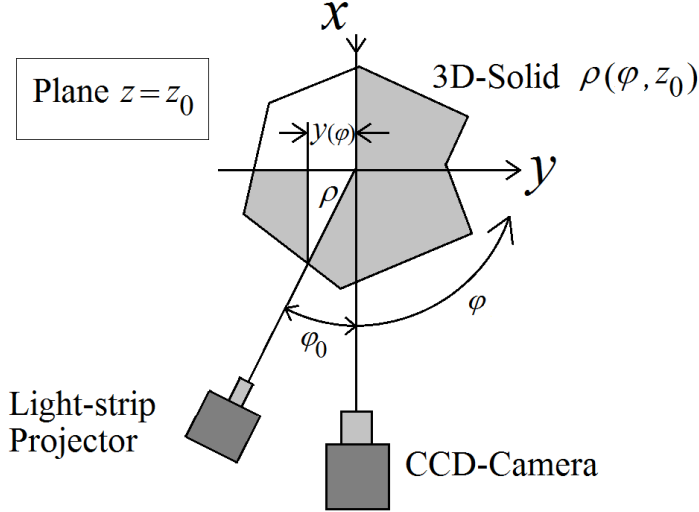


Fig. 3 This figure shows a z -cut at plane $z = z_0$ of a solid $\rho = \rho(\varphi, z)$ being digitized. The phase-displaced light-strip as seen by the camera is $\psi(\varphi) = \rho \sin(\varphi_0)$.

Once a set of N individual light-strip CCD-images (see Eq. (1)) are taken at the discrete rotation angles $n\Delta\varphi$, we proceed to form a carrier-frequency fringe-pattern $I(\varphi, z)$ of the digitizing object $\rho = \rho(\varphi, z)$ in cylindrical coordinates as, (see Fig. 4),

$$I(\varphi, z) = G(\varphi, z) + G(\varphi - \Delta\varphi, z) + G(\varphi - 2\Delta\varphi, z) + \dots + G[\varphi - (N-1)\Delta\varphi, z]; \quad \Delta\varphi = \frac{2\pi}{N}. \quad (3)$$

From Fig. 3 we see that $y = y(\varphi, z)$, so we can reduced the number of variables from $(y, z; \varphi)$ in Eq. (2) to (φ, z) in Eq. (3). Finally Eq. (3) represents the sum of N -displaced light-strip irradiances constructing a carrier-frequency fringe-pattern suitable for being analyzed by the Fourier phase-demodulation technique.

As far as we know, strip-light projection profilometry coupled to the Fourier phase-demodulation is a new contribution of this paper. In the case of reference [15] by the same authors one uses a fringe-pattern projection not light-strip projection. This makes that in [15], one needs 4 phase-shifted fringe-patterns images (4-full object rotations [15]) to demodulate the phase. This is because the fringe-patterns generated in Ref. [15] have no carrier. In contrast, in this paper, only one solid revolution generates the only carrier-frequency fringe-pattern needed.

3. Experimental carrier-fringes construction for a centered sphere covering 360-degrees

Here we show how to construct a 360-degrees carrier-frequency fringe-pattern from N -Gaussian images taken within the azimuthal range of $\varphi \in [0, 2\pi]$ (a full revolution).

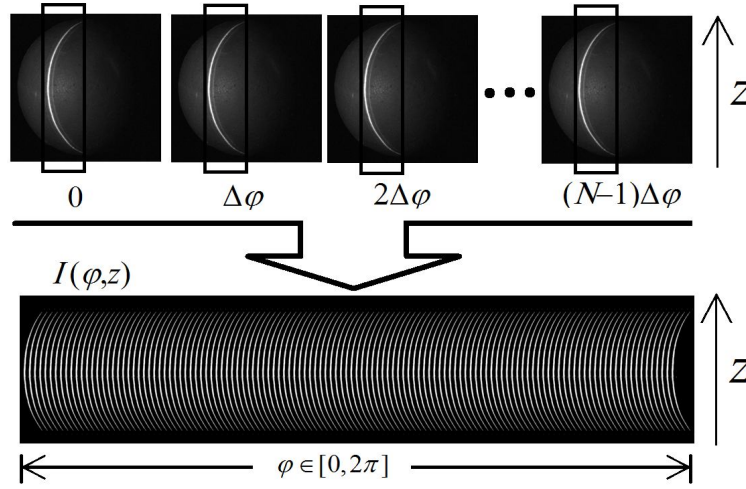


Fig. 4. 360-degrees ($\varphi \in [0, 2\pi]$) fringe-pattern construction from N digitized Gaussian light-strip images for each rotation step $\{0, \Delta\varphi, 2\Delta\varphi, \dots, (N-1)\Delta\varphi\}$. Only one fringe-pattern image constructed in this way is needed to obtain the full 360-degrees digitized sphere.

Fig. 4 shows the carrier-fringe construction process followed by our light-strip 360° profilometer. As can be seen, the carrier-frequency fringe-pattern is generated by assembling N -Gaussian strip-lights side by side to form the carrier-fringes shown. The advantage of this scheme is that a single fringe-pattern is enough to demodulate the solid's phase. This means that we do not need to take several phase-shifted fringe-patterns as we did in Ref. [15]. As mentioned, the sphere is completely covered by the strip-light without self-occluding shadows (as it would occur in Ref. [2]). In Fig. 4, all the light-strip CCD-images over the sphere look identical because the sphere is symmetric over a full revolution (360°) around the vertical line crossing its center.

4. Fourier phase-demodulation of the carrier-fringes of the proposed 360° profilometer

The function space S of the solid surfaces that can be digitized by light-strip profilometers is given by the following set of single-valued, real functions $\rho = \rho(z, \varphi)$ as,

$$S = \{ \rho = \rho(\varphi, z) \mid \rho \in [0, R], z \in [-L, L], \varphi \in [0, 2\pi) \}, \quad \rho = \sqrt{x^2 + y^2}. \quad (4)$$

The set S is bounded to $[-L, L]$ in the z -direction, to $[0, 2\pi]$ in the azimuthal φ direction, and to $[0, R]$ in the ρ direction (Fig. 1, Fig. 3). As seen in Fig. 2, the first step in our technique is to collect N images of the light-strip as imaged over the CCD-camera (Fig. 1, Fig. 2 and Fig. 3). In Fig. 2 the ambient light of the laboratory is turned-on to see the sphere, however in practice (see Fig. 4), this ambient light is turned-off. That is why the phase-modulated strip-light is the only light seen in the field of view of the CCD camera.

The sum of N displaced light-strip irradiance $G(\varphi - n\Delta\varphi, z)$ forms the fringe pattern $I(\varphi, z)$ in Fig. 4. The first harmonics of $I(\varphi, z)$ may be modeled by,

$$I(\varphi, z) = \sum_{n=0}^{N-1} G(\varphi - n\Delta\varphi, z) \approx a(\varphi, z) + b(\varphi, z) \cos[\omega_0\varphi + g\rho(\varphi, z)]. \quad (5)$$

The demodulated phase $g\rho(\varphi, z)$ gives the searched 3D-surface. The spatial-carrier ω_0 of the constructed fringes from N -light-strip images is numerically given by

$$\omega_0 = \frac{2\pi(\text{Number of strips in the } \varphi \text{ direction})}{\text{Number of pixels in the } \varphi \text{ direction}} \left(\frac{\text{radians}}{\text{pixels}} \right) \quad (6)$$

Finally the phase $g\rho(z, \varphi)$ in Eq. (5) is obtained using Fourier phase-demodulation [1]. Eq. (5) may be re-written using the exponential complex form of the cosine as,

$$I(\varphi, z) = a(\varphi, z) + \frac{b(\varphi, z)}{2} e^{i[\omega_0\varphi + g\rho(\varphi, z)]} + \frac{b(\varphi, z)}{2} e^{-i[\omega_0\varphi + g\rho(\varphi, z)]}. \quad (7)$$

Taking the Fourier transform of this signal one obtains the spectrum of the phase-modulated fringe carrier as (see Fig. 5),

$$F[I(\varphi, z)] = A(\omega_\varphi, \omega_z) + C(\omega_\varphi - \omega_0, \omega_z) + C^*(\omega_\varphi + \omega_0, \omega_z). \quad (8)$$

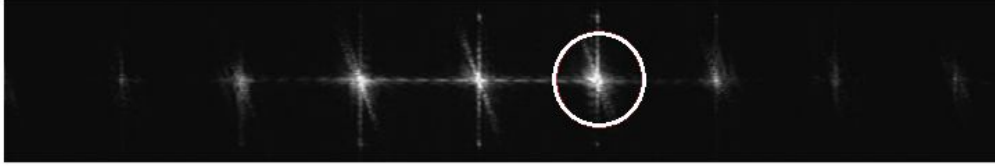


Fig. 5. This figure shows the frequency spectrum of the digitally constructed carrier-frequency fringes of the sphere shown in Fig. 4. The spectral harmonics are mainly due to the use of light-strip intensity profiles instead of a sinusoidal profile.

Where $(\omega_\varphi, \omega_z) \in [-\pi, \pi] \times [-\pi, \pi]$ is the Fourier spectrum space corresponding to the image $I(\varphi, z)$ in cylindrical coordinates (Fig. 5). The spectra $A(\omega_\varphi, \omega_z) = F[a(\varphi, z)]$ and $C(\omega_\varphi, \omega_z) = F\{(1/2)b(\varphi, z)\exp[i g\rho(\varphi, z)]\}$ are the central and right-side spectral lobes respectively. As Fig. 5 shows, the harmonics of the spectrum of $I(\varphi, z)$ are well separated so they do not interfere with the desired spectral-lobe (red-circle). The amount of harmonic distortion is minimized by locating the Gaussian light-strips in such a way that their added intensity $I(\varphi, z)$ resembles most to a sinusoidal signal. In other words, if the individual light-strips were too far away the amount of distorting harmonics would be high because the added light-strips are far from approximating a sinusoidal function. On the other hand, if the light-strips were located too close, the amplitude of the desired analytic signal would decrease. So there is a compromise between separating too-much or too-little the individual light-strip images to approximate a sinusoidal carrier-frequency fringe-pattern.

After applying the band-pass filter (the circle in Fig. 5) and displacing this spectral lobe to the spectral origin, one uses the inverse Fourier transform to obtain the desired analytic signal as,

$$F^{-1}\left[C(\omega_\varphi, \omega_z)\right] = \frac{b(\varphi, z)}{2} e^{i g \rho(\varphi, z)}. \quad (9)$$

Finally the wrapped demodulated phase $g \rho_w(\varphi, z)$ is recovered as,

$$g \rho_w(\varphi, z) = \text{angle} \left[\frac{b(\varphi, z)}{2} e^{i g \rho(\varphi, z)} \right]; \quad \rho \in [0, R], \quad z \in [-L, L], \quad \varphi \in [0, 2\pi]. \quad (10)$$

We then proceed to unwrap the demodulated phase $g \rho_w(\varphi, z)$ to obtain the continuous phase $g \rho(\varphi, z)$, still in cylindrical coordinates. The final step is the rendering of the recovered solid from cylindrical coordinates $g \rho(\varphi, z)$ into a 3D-surface in Cartesian coordinates.

5. Conclusions

Here we have presented a new algorithm for Fourier phase-demodulation applied to 360° profilometry using strip-light projection. This new algorithm combines standard Fourier phase-demodulation profilometry with standard strip-light 360° profilometry. The herein presented light-strip profilometer is capable of digitizing solids represented by single-valued, bounded surfaces $\rho = \rho(\varphi, z)$. As any other strip-light 360° profilometer, it can digitize 3D-surfaces minimizing the self-occluding shadows.

Acknowledgements

The authors would like to acknowledge the financial support from project 177044 granted by the Mexican Consejo Nacional de Ciencia y Tecnología (CONACYT).